PAPER

Check for updates

Role of sulfur vacancies in MoS₂ monolayers in stabilizing Co atoms for efficient CO oxidation†

Manman Li, Tianchun Li and Yu Jing [ID] *

By performing first-principles calculations, a MoS₂ monolayer with a Co atom doped at the sulfur defect (Co-^{S}MoS₂) was investigated as a single-atom catalyst (SAC) for CO oxidation. The Co atom is strongly constrained at the S-vacancy site of MoS₂ without forming clusters by showing a high diffusion energy barrier, ensuring good stability to catalyze CO oxidation. The CO and O₂ adsorption behavior on Co-^{S}MoS₂ surface and four reaction pathways, namely, the Eley–Rideal (ER), Langmuir–Hinshelwood (LH), trimolecular Eley–Rideal (TER) as well as the New Eley–Rideal (NER) mechanisms are studied to understand the catalytic activity of Co-^{S}MoS₂ for CO oxidation. The CO oxidation is more likely to proceed through the LH mechanism, and the energy barrier for the rate-limiting step is only 0.19 eV, smaller than that of noble metal-based SACs. Additionally, the NER mechanism is also favorable with a low energy barrier of 0.26 eV, indicating that the Co-^{S}MoS₂ catalyst can effectively promote CO oxidation at low temperatures. Our investigation demonstrates that the S-vacancy of MoS₂ plays an important role in enhancing the stability and catalytic activity of Co atoms and Co-^{S}MoS₂ is predicted to be a promising catalyst for CO oxidation.

1. Introduction

Carbon monoxide (CO), originating from deficient combustion of carbon-containing fuels (such as coal and oil) from automobiles and industrial processes, is a widely distributed toxic gas in the atmosphere and can severely poison noble metal catalysts in fuel cells.[1–3] The oxidation of CO to CO₂ at low temperature is an effective strategy to relieve the problems caused by increased CO emission.[4–7] Although the oxidation of CO is exothermic, the slow kinetics of this reaction demands the development of efficient catalysts to reduce the activation barrier.[8] In the past decades, noble metal catalysts, such as Pt,[9,10] Au,[11,12] Pd,[13,14] and Rh[15,16] have been extensively explored and exhibit good catalytic activity for CO oxidation. However, these catalysts are expensive and typically require high reaction temperatures to operate efficiently, which prevents their large-scale commercial applications.[13] Therefore, low-cost and efficient non-noble metal-based catalysts are highly demanded.

In 2011, the preparation of homogeneous single Pt atoms on FeO$_X$ was first reported, and the Pt/FeO$_X$ catalysts showed good catalytic performance for CO oxidation.[17] Thereafter, single-atom catalysts (SACs) have been rapidly developed as an important class of catalysts by showing good catalytic activity

and selectivity for many reactions including CO oxidation,[18,19] oxygen reduction reactions (ORR),[20,21] oxygen evolution reactions (OER),[22,23] and hydrogen evolution reactions (HER).[24,25] In contrast to conventional bulk metal catalysts, SACs are supported catalysts containing individual atoms isolated from each other as active centers, maximizing the utilization efficiency of metal atoms and reducing the cost.[26] However, the isolated single metal atoms prone to be aggregated because of their high surface free energy and stable support materials are crucial to obtaining stable SACs with finely dispersed metal centers.

Recently, 2D materials have been widely studied as SAC supports because of their large surface area, tunable electronic properties and good stability, and some 2D SACs have been demonstrated to be promising catalysts for CO oxidation.[27–34] Among them, 2D transition metal dichalcogenides (TMDCs) represented by MoS₂ monolayers have drawn broad research interests because of their good stability and high experimental accessibility.[35–38] Previous studies have demonstrated that doping transition metals on MoS₂ monolayer can effectively tune the electronic structure and magnetic properties of MoS₂,[39] significantly enhancing the interaction between the catalyst and the adsorbed CO and O₂ to facilitate CO oxidation.[40–42] For instance, MoS₂ monolayers with Co-doped on the pristine surface was demonstrated to show high catalytic activity for CO oxidation.[43] However, aggregation of Co on pristine MoS₂ will be inevitable due to the weak interaction between Co and the defect-free surface. In fact, the embedding of non-precious metals in the S vacancy of MoS₂ can be experimentally

Jiangsu Co-Innovation Centre of Efficient Processing and Utilization of Forest Resources, College of Chemical Engineering, Nanjing Forestry University, Nanjing 210037, China. E-mail: yujing@njfu.edu.cn

† Electronic supplementary information (ESI) available. See DOI: https://doi.org/10.1039/d2ra06261e

feasible,[44,45] because when 2D MoS$_2$ was prepared using mechanical exfoliation or chemical vapor deposition techniques, S vacancies were the predominant defects and can even be controlled by using low-energy argon sputtering or electron irradiation techniques.[46–48] Recently, Liu *et al.* synthesized MoS$_2$ monolayer with cobalt-embedded at the sulfur vacancies by mixing chemically exfoliated MoS$_2$ monolayer containing S vacancies with thiourea-like cobalt complexes,[49] which exhibited high activity and stability for hydrodeoxygenation reaction and formaldehyde oxidation.[50] Inspired by the good stability and high synthesizing feasibility of MoS$_2$ monolayers with Co embedded in the sulfur vacancies, it is rather appealing to investigate their catalytic performance for CO oxidation, which has not been explored before.

In this work, we performed first-principles calculations to study the potential of MoS$_2$ monolayers with individual Co atom embedded in the S vacancy (Co-^{S}MoS$_2$) as SACs for CO oxidation. The stability of Co-^{S}MoS$_2$ was first verified by estimating the diffusion of Co from the S vacancy to different adjacent surface sites. Then, the adsorption of CO and O$_2$ on Co-^{S}MoS$_2$ was examined in comparison with that on defect-free MoS$_2$ monolayer, defect-free MoS$_2$ monolayer with a single Co atom decorated on the surface (Co/MoS$_2$) and MoS$_2$ monolayer containing S vacancies (MoS$_2$-Sv). Four CO oxidation mechanisms on the Co-^{S}MoS$_2$, including, Eley–Rideal (ER), New Eley–Rideal (NER), Langmuir–Hinshelwood (LH) and trimolecular Eley–Rideal (TER) mechanisms, were systematically explored. The results indicate that Co-^{S}MoS$_2$ can facilitate CO oxidation through the LH and NER mechanisms by surmounting small energy barriers and show superior stability and catalytic activity than other examined MoS$_2$ based structures because of the strong interaction between Co and sulfur vacancy, thus is predicted to be a promising catalyst for CO oxidation.

2. Computational methods

All calculations were carried out with the projected augmented wave (PAW) potential of spin-polarized density functional theory (DFT), as implemented in the Vienna Ab initio Simulation Package (VASP).[51–53] The generalized gradient approximation (GGA) method with Perdew–Burke–Ernzerhof (PBE) was adopted to depict exchange–correlation potential.[54] The van der Waals (vdWs) interactions between the adsorbing molecules and the monolayer were depicted by using the DFT-D3 method proposed by Grimme.[55] The plane-wave cutoff energy was set as 420 eV and the Monkhorst–Pack grid of $3 \times 3 \times 1$ and $5 \times 5 \times 1$ k-points grid were used for the geometry optimization and the calculation of electronic properties. The system is considered to be self-consistent when the total energy and the magnitude of the force on each atom are below 10^{-5} eV and 0.01 eV Å^{-1}, respectively. The vacuum layer of the MoS$_2$ monolayer was set to be 20 Å to avoid interlayer interactions. The minimum energy paths for CO oxidation reaction were searched by the climbing image nudged elastic band (CI-NEB) and dimer method,[56–58] and the transition state (TS) geometries were obtained after vibrational analysis. The lattice parameter of MoS$_2$ monolayer was optimized to be 3.17 Å, which agrees well with the results of

previously experimental and theoretical studies.[43,59] The binding energy (E_b) of Co atom in Co-^{S}MoS$_2$ was calculated by

$$E_b = E_{\text{Co-}^S\text{MoS}_2} - E_{\text{MoS}_2\text{-Sv}} - E_{\text{Co}} \quad (1)$$

where $E_{\text{Co-}^S\text{MoS}_2}$, $E_{\text{MoS}_2\text{-Sv}}$, and E_{Co} are the total energy of the defective MoS$_2$ embedded with a Co atom, MoS$_2$ with a S vacancy and the free Co atom, respectively.

The adsorption energy (E_{ads}) of different adsorbates on different substrates was calculated according to

$$E_{\text{ads}} = E_{\text{sub+gas}} - E_{\text{sub}} - E_{\text{gas}} \quad (2)$$

where $E_{\text{sub+gas}}$, E_{sub} and E_{gas} represent the total energies of the substrate adsorbed with gas molecule, the bare substrate and the free gas molecule, respectively. A more negative E_{ads} value indicates a more favorable adsorption of the gas molecule.

To investigate whether the CO oxidation performance is affected by the doping concentration of Co, we constructed a 2×2, 3×3, 4×4 and 5×5 supercell containing one Co atom embedded at the S vacancy, corresponding to the atomic embedding concentration of 25%, 11%, 6% and 4%, respectively. However, it turned out that these four supercells gave identical E_b values of Co and E_{ads} for CO and O$_2$ (Table S1†), indicating that the concentration of Co shows negligible influence on their catalytic activity. Therefore, considering the computational accuracy and efficiency, the 4×4 MoS$_2$ supercell is used for all catalysis calculations unless stated otherwise.

The reaction energy barriers (E_{bar}) and reaction energy (ΔE) for the elementary steps of CO oxidation reaction was defined as

$$E_{\text{bar}} = E_{\text{TS}} - E_{\text{IS}} \quad (3)$$

$$\Delta E = E_{\text{FS}} - E_{\text{IS}} \quad (4)$$

where E_{TS}, E_{IS} and E_{FS} denote the energy of the TS, initial state (IS) and final state (FS), respectively. A more positive ΔE value indicates a more endothermic reaction process, while a negative value represents an exothermic reaction.

3. Results and discussion

3.1 Structure and stability of Co-^{S}MoS$_2$

The structural and electronic properties of Co-^{S}MoS$_2$ were first studied. As shown in Fig. 1a, the Co atom is embedded at the S vacancy forming three covalent bonds with its adjacent Mo atoms and the average bond length of Co–Mo is 2.51 Å. The E_b of Co atom is −4.39 eV, indicating a strong interaction of Co atom with the neighboring Mo atoms, which is stronger than that on the defect-free MoS$_2$ surface (−3.28 eV). In view of the cohesion energy of bulk Co (−4.39 eV),[60] it can be expected that the embedded Co atoms are less likely to aggregate to form large clusters on defective MoS$_2$ compared to the defect-free surface. To gain a deep understanding of the stability of Co-^{S}MoS$_2$, we estimated the migration of Co atom from the S vacancy to a nearby hollow site. As shown in Fig. 1b, the calculated diffusion process is endothermic (1.26 eV) with a high diffusion energy barrier of 1.71 eV. In contrast, the E_b of Co atom on two different surface
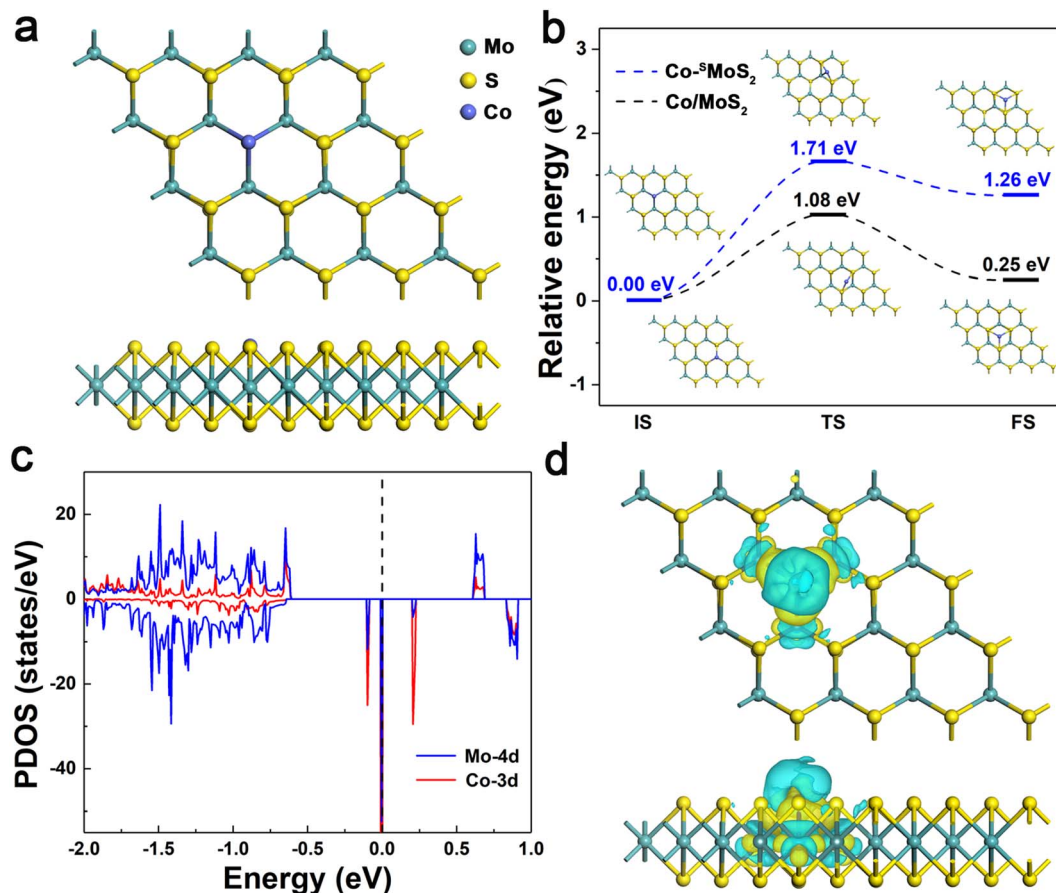
Fig. 1 (a) Top and side views of optimized Co-^{S}MoS$_2$. (b) The IS, TS and FS geometries of Co-^{S}MoS$_2$ (blue line) and Co/MoS$_2$ (black line) along the diffusion path for Co atom migrating from the S vacancy and Mo-top site to the nearby hollow site, respectively. (c) The PDOS of Co-3d (red curve) and Mo-4d (blue curve) states for Co-^{S}MoS$_2$. The Fermi level is set to zero. (d) CDD for Co-^{S}MoS$_2$, yellow and cyan areas indicate charge accumulation and depletion, respectively. The isosurface value is set as 0.0018 e/bohr^3.

sites of defect-free MoS$_2$ only differs in 0.25 eV and the diffusion energy barrier of Co is 1.08 eV. The results suggest that the S vacancies on MoS$_2$ play an important role in stabilizing the Co atoms and inhibiting their further aggregation.

The spin polarized partial density of states (PDOS) projected on the Co-3d and adjacent Mo-4d orbitals were plotted in comparison with the total DOS to understand the electronic structure of Co-^{S}MoS$_2$. As shown in Fig. 1c, the embedding of Co atom induces impurity states around the Fermi energy level, contributing to a reduced band gap (0.20 eV) of Co-^{S}MoS$_2$ compared to the pristine MoS$_2$ monolayer. The pronounced hybridization between the Co-3d orbital and the adjacent Mo-4d orbitals around the Fermi energy level is responsible for the strong interaction between Co and defective MoS$_2$. Bader charge analysis[61] shows that there is about 0.14|e| charge transferred from the Co atom to the adjacent Mo atoms, which can be visualized by the charge density difference (CDD) analysis. As illustrated in Fig. 1d, there is obvious electron depletion (cyan) and electron accumulation (yellow) at the Co and the neighboring Mo atoms, respectively. The strong interaction and significant charge reallocation between Co and defective MoS$_2$ will favor the good stability and high activity of Co-^{S}MoS$_2$ for efficient CO oxidation.

3.2 Activation of gas molecules on different MoS$_2$ monolayers

Before exploring the mechanism of CO oxidation on Co-^{S}MoS$_2$ surfaces, the adsorption and co-adsorption of the reactants (CO and O$_2$) were first examined. The most preferred adsorption site for each molecule was decided by considering different adsorption configurations. The CO molecule prefers to be adsorbed at the Co site of Co-^{S}MoS$_2$ with the end-on configuration, as exhibited in Fig. 2a. The calculated E_{ads} is −1.78 eV and the bond length of Co–C is 1.79 Å, indicating a strong interaction between the adsorbed CO and the Co-^{S}MoS$_2$. Bader charge analysis indicates about 0.20|e| charge transferred from Co-^{S}MoS$_2$ to CO and CDD analysis (Fig. 2b) illustrates the electron accumulation at the Co–C bond. The PDOS analysis (Fig. S2a, ESI†) shows that there is obvious hybridization between the Co-3d orbital and the C-2p and O-2p orbitals near the Fermi level. The significant charge transfer and strong hybridization between Co atoms and the adsorbed CO molecule indicate that the CO molecule can been effectively activated by the Co, leading to elongated C–O bond from 1.14 to 1.16 Å.

The most stable adsorption configuration of O$_2$ on Co-^{S}MoS$_2$ can be seen in Fig. 2c. It can be found that the O$_2$ molecule is
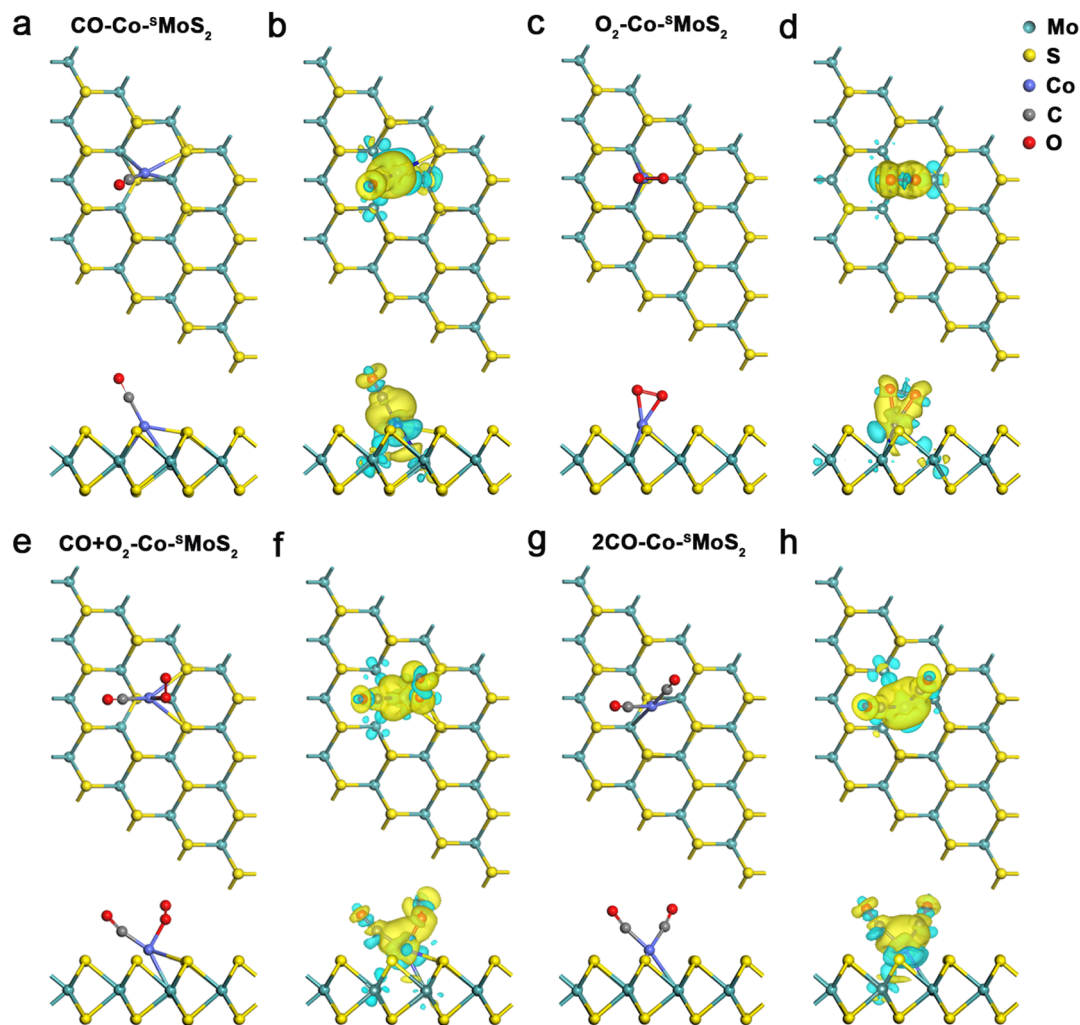
Fig. 2 Top and side views of the optimized structure and CDD of CO (a and b), O_2 (c and d) CO + O_2 (e and f) and 2CO (g and h) adsorbed Co-^{S}MoS$_2$. Yellow and cyan areas denote charge accumulation and depletion, respectively. The isosurface value is set as 0.002 e/bohr^3.

adsorbed at the Co site in a side-on manner, forming two Co–O bonds with the bond length of 1.89 Å, and the calculated E_{ads} of −1.64 eV is a little lower than that of CO. The Bader charge analysis shows that there is about 0.46|e| charge transferred from the Co-^{S}MoS$_2$ to O_2, which will occupy the 2π* orbital of O_2 and contribute to the elongation of the O–O bond from 1.23 to 1.36 Å. As shown in Fig. 2d, there is significant electron accumulation at the adsorbed O_2. These results indicate that the O_2 can be highly activated at the Co site of Co-^{S}MoS$_2$. Moreover, the hybridization (Fig. S2b, ESI†) between the Co-3d state and the O_2-2p state also suggests the significant interaction of Co atom with the adsorbed O_2 molecule.

The adsorption of CO and O_2 on defect-free MoS$_2$, Co/MoS$_2$ and MoS$_2$-Sv surfaces (Fig. S3 and Table S2, ESI†) were also examined as comparisons. It can be found that the adsorption of CO and O_2 on defect-free MoS$_2$ is rather weak and the E_{ads} is as small as −0.15 and −0.09 eV, respectively. Thus, CO and O_2 can only be physisorbed on defect-free MoS$_2$ monolayer. On the MoS$_2$-Sv surface, CO and O_2 molecules are adsorbed at the S vacancy in an end-on and side-on manner, respectively. The C–

O bond of CO and the O–O bond of O_2 is elongated to 1.16 and 1.44 Å and the E_{ads} is −1.24 and −2.14 eV, respectively. Therefore, the S vacancy of MoS$_2$-Sv prefers to be occupied by O_2 instead of CO. On the Co/MoS$_2$ surface, the E_{ads} of CO and O_2 is −2.30 and −1.90 eV, respectively, and the C–O and O–O bond length increase to 1.16 and 1.35 Å, respectively. It can be found that surface defects play important roles in enhancing the ability of MoS$_2$ monolayer to activate surface molecules and different kinds of defects contribute to different activation of CO and O_2, which will result in different catalytic performances for CO oxidation.

To better reveal the mechanism of CO oxidation reaction on the surface of different catalysts, the co-adsorption of the reactants is also investigated because the preferred adsorption manner can determine the pathway of CO oxidation. Fig. 2e and g show the most stable co-adsorption configurations of CO + O_2 and two CO molecules on Co-^{S}MoS$_2$, respectively. The co-adsorption energy of CO + O_2 is calculated to be −2.04 eV, more negative than that of the isolate adsorption of CO or O_2, indicating that co-adsorption of CO + O_2 molecules on

Co-^{S}MoS$_2$ is more favored. The co-adsorption of two CO molecules is also examined which turns out to be more favorable than that of one CO molecule alone, where a V-type OCCoCO structure was formed with an E_{ads} of −2.81 eV. There is an obvious charge accumulation and depletion between the Co atom and the adsorbed CO + O$_2$ or 2CO molecules (Fig. 2f and h). Thus, in terms of E_{ads}, the co-adsorption of 2CO molecules is even more feasible than that of CO + O$_2$ molecules on Co-^{S}MoS$_2$.

For the defect-free MoS$_2$, the adsorption of CO + O$_2$ and 2CO remains weak with the E_{ads} of −0.28 eV and −0.33 eV, respectively (Fig. S4a and Table S2, ESI†); for the MoS$_2$-Sv surface, the second gas molecule is difficult to be adsorbed after the adsorption of one molecule of CO or O$_2$ on the S vacancy (Fig. S4b, ESI†), indicating that the S vacancy tends to be oxidized at the exposure of CO or O$_2$, which will cause catalyst deactivation. Thus we further examined the robustness of MoS$_2$-Sv by estimating the feasibility of removing the O* species at the S vacancy using a molecule of CO (Fig. S5, ESI†). The results show that this step (CO + O* → CO$_2$) requires to conquer a high energy barrier of 2.17 eV and this elementary reaction is endothermic with the reaction energy of 0.83 eV, indicating that the O* species is difficult to be removed and the S vacancy will be definitely poisoned. The co-adsorption configurations of CO + O$_2$ and 2CO on Co/MoS$_2$ are similar to those on Co-^{S}MoS$_2$ and exhibit the E_{ads} of −2.67 and −3.29 eV, respectively (Fig. S4c, ESI†). Since defect-free MoS$_2$ shows weak adsorption of the reactants and MoS$_2$-Sv tends to be oxidized by the reactants, they are both unfavorable for subsequent CO oxidation, and thus are excluded from potential catalysts for further discussion. We only examined the detailed CO oxidation process on Co-^{S}MoS$_2$ and Co/MoS$_2$ in subsequent calculations unless stated otherwise.

The E_{ads} of CO$_2$ on Co-^{S}MoS$_2$ and Co/MoS$_2$ was then examined since CO$_2$ is the final product of CO oxidation, which turns out to be −0.48 eV for both cases (Fig. S3c, d and Table S2, ESI†).

This indicates that the adsorption of CO$_2$ molecule on Co-^{S}MoS$_2$ and Co/MoS$_2$ is feeble and can be desorbed from the surface site at room temperature. Furthermore, when the free O$_2$ or CO molecules approach to the Co-^{S}MoS$_2$ with CO$_2$ pre-adsorbed, the CO$_2$ is automatically desorbed from the catalyst (Fig. S6, ESI†). Thus, even in the presence of abundant CO$_2$, O$_2$ and CO molecules can still reoccupy the active site to promote the next step of CO oxidation.

3.3 CO oxidation over Co-^{S}MoS$_2$

Generally, CO oxidation reactions can occur through three traditional pathways, namely, the ER, LH, and TER mechanisms,[28,33] which are determined by the initial adsorption configuration of the reactant molecules. For the ER mechanism, O$_2$ is pre-adsorbed at the reaction site, following by the approaching of CO to form the CO$_3$* intermediates (IM) or directly to produce a CO$_2$, leaving a O* species. The LH mechanism is facilitated by the co-adsorption of CO and O$_2$ molecules at the reaction site to form peroxide-like OOCO* complexes, which then dissociate into CO$_2$ and O*. The TER mechanism will proceed when the O$_2$ reacts with the co-adsorbed bi-molecular CO to form OCOOCO* (IM), which subsequently turns into two CO$_2$ molecules. As mentioned in Section 3.2, the adsorption energy of CO (−1.78 eV) and O$_2$ (−1.64 eV) on Co-^{S}MoS$_2$ are similar, so that different reactants may be adsorbed at the active site when the reactant concentrations vary, and we next discuss the possible reaction mechanisms for different reactant concentrations.

3.3.1 ER mechanism. If the concentration of O$_2$ is larger than that of CO, CO oxidation will proceed *via* the ER mechanism. In the first step, the energetically preferred O$_2$ adsorption structure was chosen as the IS (Fig. 3). As the CO approaches to
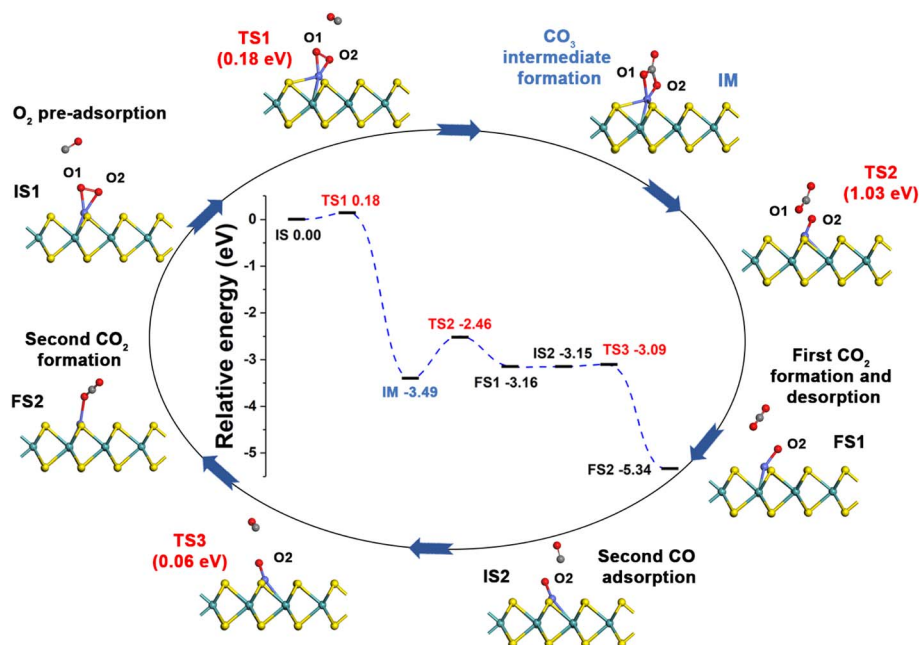

Fig. 3 Reaction pathway for CO oxidation on Co-^{S}MoS$_2$ through the ER mechanism.

the Co-^{S}MoS$_2$ with O$_2$ preadsorbed (TS1), the O1–O2 bond of O$_2$ will be activated and then broken after CO is combined, forming a carbonate-like CO$_3$* (IM). This step (CO + O$_2$* → CO$_3$*) on Co-^{S}MoS$_2$ is exothermic with the reaction energy of −3.49 eV and the energy barrier is as small as 0.18 eV. The C–O bond of CO in IM is extended to 1.21 Å and the C–O1/O2 bond length is about 1.35 Å. Meanwhile, the Co–O1 and Co–O2 bond distance is decreased to 1.92 and 1.86 Å, respectively. In the second step, with elongation of the C–O1 and Co–O1 bonds, the IM decomposes into CO$_2$ and O* (FS1) through TS2. This step (CO$_3$* → CO$_2$ + O*) is endothermic by 0.33 eV and shows an energy barrier of 1.03 eV. Then the first CO$_2$ molecule is formed and released, leaving an O* species stabilized on the Co site (FS1). Subsequently, the second CO molecule approaches to the O* species to form a second CO$_2$ (CO + O* → CO$_2$) through TS3 with the reaction energy of −2.19 eV and a very small energy barrier of 0.06 eV. It can be found that the second step (CO$_3$* → CO$_2$ + O*) is the rate-determining step (RDS) and IM is more stable than IS and FS1, which is thermodynamically unfavorable, and the high energy barrier makes it kinetically infeasible to proceed through the ER mechanism.

3.3.2 NER mechanism. Recently, a new mechanism based on the pre-adsorption of O$_2$, namely the NER mechanism has been proposed for CO oxidation,[62,63] which indicates that two CO molecules can simultaneously attack the adsorbed O$_2$, facilitating the breakage of the O–O bond to produce two CO$_2$ molecules. Here, the NER mechanism was examined by using the configuration of two physisorbed CO molecules on the pre-adsorbed O$_2$ over Co-^{S}MoS$_2$ as the IS (Fig. 4). The initial distance between the C atom of CO and O of O$_2$ is about 3.17 Å and the O–O bond length is 1.36 Å. As the distance between CO and O$_2$

reduces gradually, the O–O bond is elongated from 1.36 to 2.49 Å, leading to the bond breakage and the formation of two new C–O bonds, forming a pentagonal ring of OOCCOO* (IM) through TS1. This step (2CO + O$_2$* → OOCCOO*) is exothermic with the reaction energy of −4.05 eV and shows a rather low energy barrier of 0.08 eV. As the C–C bond breaks, the IM is segregated into two CO$_2$ molecules (FS) by overcoming an energy barrier of 0.26 eV (TS2) and the reaction energy of this step (OOCCOO* → 2CO$_2$) is −1.30 eV, which turns out to be the RDS along the NER mechanism. After two CO$_2$ molecules are released, the Co-^{S}MoS$_2$ catalyst can be refreshed for further CO oxidation cycles.

3.3.3 LH mechanism. CO oxidation will proceed through the LH mechanism if the concentrations of CO and O$_2$ are about equal. As discussed above, the co-adsorption energy of CO + O$_2$ molecules on Co-^{S}MoS$_2$ (−2.04 eV) is more negative than that of the isolated adsorption of CO or O$_2$, indicating the high feasibility of the LH mechanism. The geometric structure and energy profile of different intermediates of the LH mechanism are presented in Fig. 5. The reaction is initiated with the most favorable co-adsorption of O$_2$ and CO on Co-^{S}MoS$_2$ (IS1), where the O$_2$ and CO are both adsorbed in an end-on manner. The bond length of O1–O2 in O$_2$ and C–O in CO is slightly elongated to 1.29 and 1.16 Å, respectively, indicating that both CO and O$_2$ molecules are activated. Then, CO and O$_2$ are rotated with O$_1$ gradually approaching the C atom, contributing to the shortened distance between the CO and O$_2$ molecules (TS1). After overcoming a small energy barrier of 0.19 eV, a carbonate-like OOCO* species is formed and the O1–O2 bond is extended to 1.53 Å while the C–O1 bond length is shortened from 2.94 to 1.34 Å. This step (CO* + O$_2$* → OOCO*) is
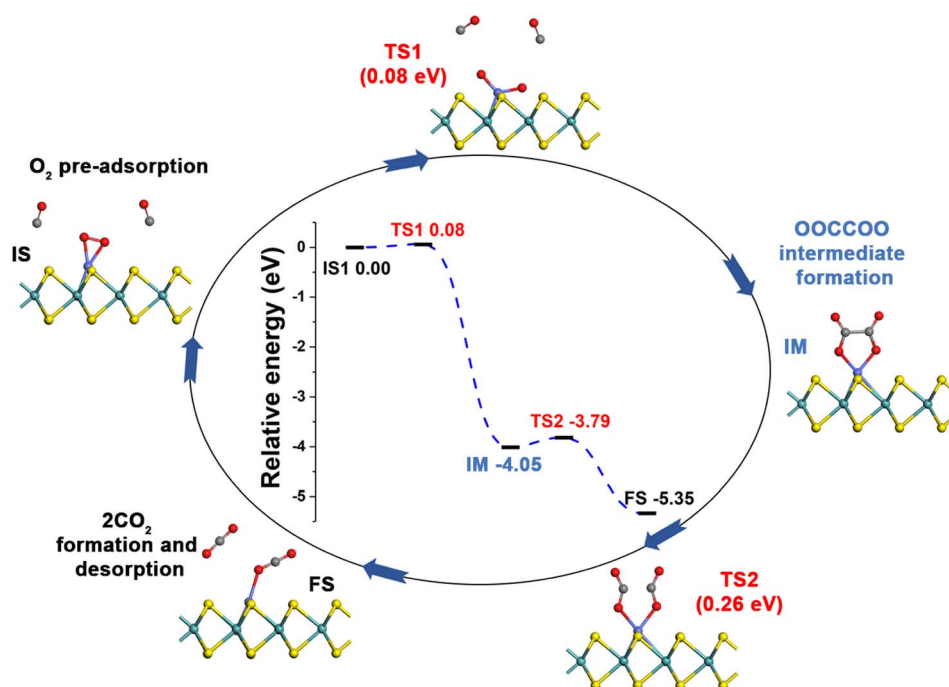

Fig. 4 Reaction pathway for CO oxidation on Co-^{S}MoS$_2$ through the NER mechanism.
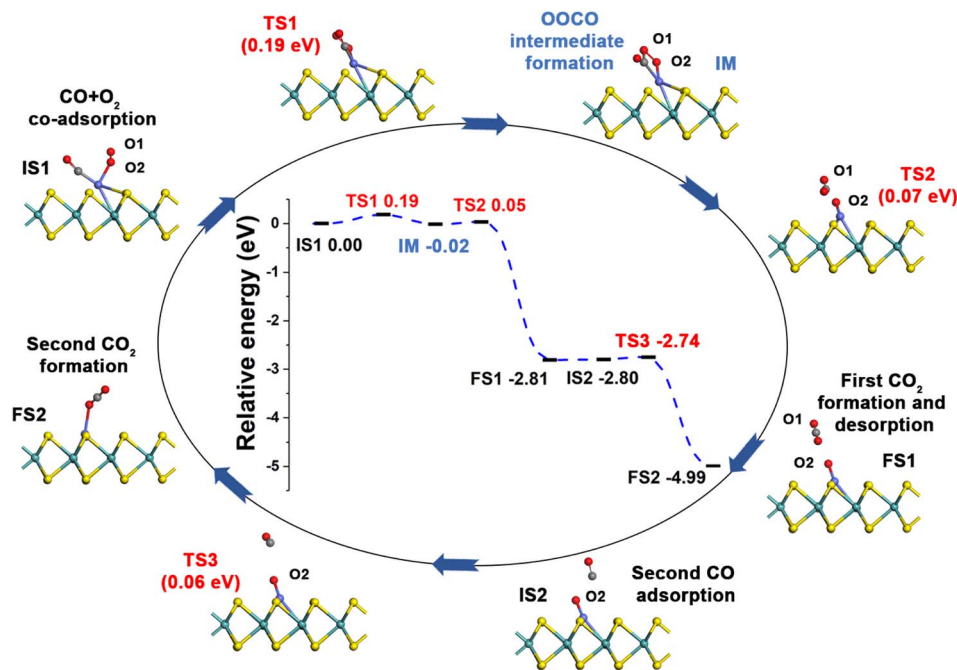
Fig. 5 Reaction pathway for CO oxidation on Co-^{S}MoS$_2$ *via* the LH mechanism.

exothermic with a reaction energy of -0.02 eV. The O$_1$–O$_2$ bond is continuously elongated, forming the first CO$_2$ molecule through TS2, leaving a O* species attached to the Co atom (FS1). This step (OOCO* → CO$_2$ + O*) is exothermic by showing a reaction energy of -2.79 eV and the energy barrier is 0.07 eV. Then, the step of generating the second CO$_2$ (CO + O* → CO$_2$) is consistent with that of the ER mechanism with the reaction energy of -2.19 eV and an energy barrier of 0.06 eV. The RDS is the step of IM generation with a rather small energy barrier of 0.19 eV for the LH mechanism, indicating that CO oxidation can proceed favorably through this pathway.

3.3.4 TER mechanism. When the concentration of CO is larger than that of O$_2$, CO oxidation will proceed through the TER mechanism. Since the co-adsorption energy of two CO molecules (-2.81 eV) are also more negative than that of the separated adsorption of CO and O$_2$, the TER mechanism can be also feasible. Fig. 6 shows the reaction diagram of CO oxidation *via* the TER mechanism. We took the configuration of O$_2$ molecules above the two co-adsorbed CO molecules as the IS1, where the bond lengths between two O of O$_2$ and two C of two CO are 4.02 Å and 3.70 Å, respectively. As the O$_2$ molecule approaches to the co-adsorbed CO molecules, the O–O bond is elongated from 1.23 to 1.49 Å, forming a pentagonal ring structure of OCOOCO* (IM) through TS1. This step (O$_2$ + 2CO* → OCOOCO*) is exothermic by showing a reaction energy of -0.26 eV and an energy barrier of 0.75 eV. Then, as the O–O bond breaks, IM dissociates to form two CO$_2$ molecules (OCOOCO* → 2CO$_2$) through TS2 by overcoming an energy barrier of 0.51 eV, and the reaction is exothermic with a reaction energy of -4.21 eV. It is noticed that the IM generation step is the RDS of the TER mechanism, which shows a higher energy

barrier (0.75 eV) than the LH (0.19 eV) and NER mechanisms (0.26 eV).

After examining all the four possible mechanisms for CO oxidation on Co-^{S}MoS$_2$ monolayer, namely ER, LH, TER and NER mechanisms, we found the LH mechanism to be most favorable pathway for CO oxidation, showing the smallest energy barrier of 0.19 eV, followed by the NER mechanism (0.26 eV). Remarkably, the three pathways, namely NER, LH and TER, all show the RDS energy barrier well below 1.0 eV, indicating that CO oxidation can be facilitated on the surface of Co-^{S}MoS$_2$ at low temperatures. The performance of Co/MoS$_2$ monolayer is finally examined as a comparison of Co-^{S}MoS$_2$. It can be found that the LH mechanism (Fig. S7, ESI†) is also the most preferred pathway for CO oxidation on Co/MoS$_2$ by showing an energy barrier of 0.62 eV. These results are highly consistent with those of the previous study (LH, 0.57 eV)[43] demonstrating the reliability of our calculations. As a result, our investigations indicate that Co-^{S}MoS$_2$ is a promising catalyst for CO oxidation and shows better stability and catalytic activity than that of Co/MoS$_2$.

The preferred LH mechanism for CO oxidation on Co-^{S}MoS$_2$ can be understood by analyzing the PDOS of the IS1 and TS1 structures along the LH mechanism on Co-^{S}MoS$_2$ (Fig. S8, ESI†). As shown in Fig. S8a,† the $2\pi^*$ orbital of the adsorbed O$_2$ is partially occupied and Bader charge analysis indicates that there is about $0.36|e|$ charge transferred from Co to O$_2$, indicating that the O–O bond is activated by Co of Co-^{S}MoS$_2$. In addition, there is a significant overlap between the $5\sigma^*$ and $2\pi^*$ states of O$_2$ and the states of Co atom, demonstrating the strong interaction between O$_2$ and Co. From IS1 to TS1, there is about $0.03|e|$ charge transfer from CO to O$_2$ and the $5\sigma^*$ state of O$_2$
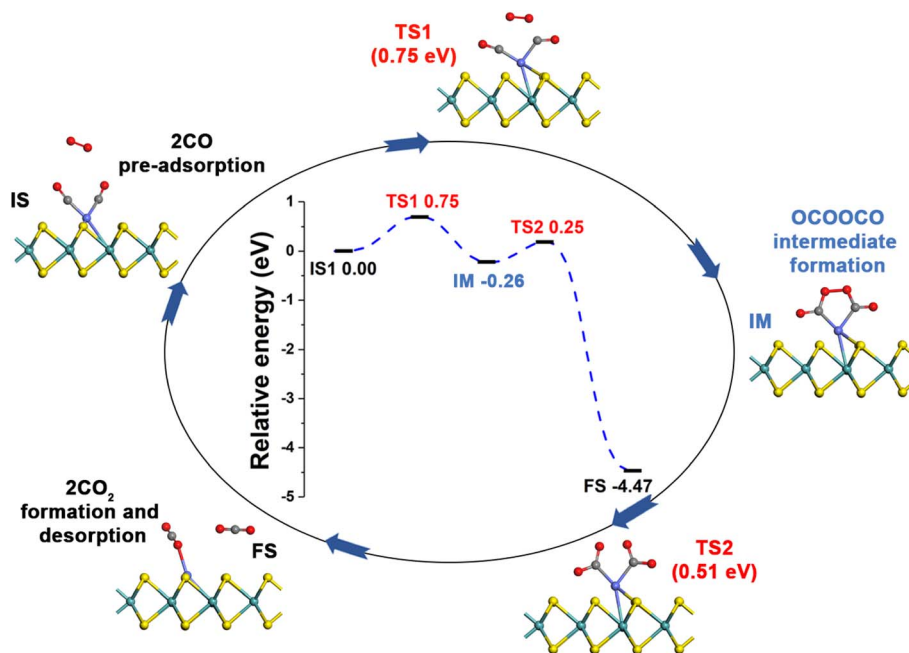
Fig. 6 Reaction pathway for CO oxidation on Co-^{S}MoS$_2$ based on the TER mechanism.

partially shifts closer to the Fermi level (Fig. S8b†). These results indicate that the co-adsorption of CO can further weaken the O1–O2 bond O$_2$. It can also be found that the 5σ and 1π states of CO and O$_2$ are broadened, indicating the formation of OCOO (IM). The above results indicate that the LH mechanism is favored by the activation of the O1–O2 bond by the embedded Co atom and the co-adsorbed CO.

To better evaluate the catalytic activity of Co-^{S}MoS$_2$ for CO oxidation, we compared the performance of Co-^{S}MoS$_2$ with that of other noble metal-based SACs and the energy barriers of the RDS over various catalysts are presented in Table 1. The energy barrier for CO oxidation on Co-^{S}MoS$_2$ can be found to be lower than that of other reported noble metal-based SACs, indicating that Co-^{S}MoS$_2$ is a highly promising SAC candidate for CO oxidation by showing higher catalytic activity and lower cost than many noble metal-based SACs.

Table 1 The energy barriers for the RDS of the most favorable mechanism of CO oxidation on Co-^{S}MoS$_2$ in comparison with that on various noble metal-based SACs

Catalyst	Barrier (eV)	Mechanism	Ref.
Co-^{S}MoS$_2$	0.19	LH	This work
Co/MoS$_2$	0.57	LH	43
Pt-graphene	0.59	LH	64
Pd-graphene	0.20	LH	65
Au-graphene	0.31	LH	66
Pd-BN nanosheet	0.35	TER	67
Au-BN	0.47	LH	34
Pd-BN	0.39	TER	68
Pt-GO	0.76	LH	69
Ir-graphdiyne	0.37	NER	70

4. Conclusions

As a summary, by performing DFT calculations, we have studied the possibility of using Co-embedded MoS$_2$ monolayers as SACs for CO oxidation. The results show that Co atoms embedded at the S vacancies of MoS$_2$ can form stable SACs without aggregating due to the strong hybridization between Co and Mo atoms, which is more robust than the Co doped defect-free MoS$_2$ surface. The adsorption manner of CO and O$_2$ molecules on Co-^{S}MoS$_2$ can decide the reaction pathway of CO oxidation and the co-adsorption of CO + O$_2$ and two CO are both favorable at the Co site of Co-^{S}MoS$_2$. The four possible reaction pathways, including ER, LH, TER and NER mechanisms for CO oxidation on Co-^{S}MoS$_2$ were discussed and the results show that the oxidation of CO can be facilitated through the LH mechanism by overcoming a small energy barrier of 0.19 eV, which is superior to many noble-metal based SACs. By exhibiting good stability, high catalytic activity, and low-cost characteristics, Co-^{S}MoS$_2$ is predicted to serve as a promising non-noble metal-based SAC candidate for efficient catalytic CO oxidation. Since Co-^{S}MoS$_2$ have been experimentally synthesized, the practice of using this material for CO oxidation can be expected in the near future.

Conflicts of interest

There are no conflicts to declare.

Acknowledgements

© 2022 The Author(s). Published by the Royal Society of Chemistry

References

1 J. J. Baschuk and X. Li, *Int. J. Energy Res.*, 2001, **25**, 695–713.
2 F. Mariño, C. Descorme and D. Duprez, *Appl. Catal., B*, 2004, **54**, 59–66.
3 L. Birry, J. H. Zagal and J.-P. Dodelet, *Electrochem. Commun.*, 2010, **12**, 628–631.
4 L. Cao, W. Liu, Q. Luo, R. Yin, B. Wang, J. Weissenrieder, M. Soldemo, H. Yan, Y. Lin, Z. Sun, C. Ma, W. Zhang, S. Chen, H. Wang, Q. Guan, T. Yao, S. Wei, J. Yang and J. Lu, *Nature*, 2019, **565**, 631–635.
5 H. Zhang, S. Fang and Y. H. Hu, *Catal. Rev.: Sci. Eng.*, 2022, **64**, 491–532.
6 B. Qiao, J. Liu, Y.-G. Wang, Q. Lin, X. Liu, A. Wang, J. Li, T. Zhang and J. Liu, *ACS Catal.*, 2015, **5**, 6249–6254.
7 H. Su and Y. H. Hu, *Chem. Eng. J.*, 2020, **402**, 126235.
8 T. Bunluesin, H. Cordatos and R. J. Gorte, *J. Catal.*, 1995, **157**, 222–226.
9 A. Alavi, P. Hu, T. Deutsch, P. L. Silvestrelli and J. Hutter, *Phys. Rev. Lett.*, 1998, **80**, 3650–3653.
10 A. Beniya, S. Higashi, N. Ohba, R. Jinnouchi, H. Hirata and Y. Watanabe, *Nat. Commun.*, 2020, **11**, 1888.
11 Y. G. Wang, Y. Yoon, V. A. Glezakou, J. Li and R. Rousseau, *J. Am. Chem. Soc.*, 2013, **135**, 10673–10683.
12 L. Li, Y. Gao, H. Li, Y. Zhao, Y. Pei, Z. Chen and X. C. Zeng, *J. Am. Chem. Soc.*, 2013, **135**, 19336–19346.
13 C. J. Zhang and P. Hu, *J. Am. Chem. Soc.*, 2001, **123**, 1166–1172.
14 F. C. H. Lim, J. Zhang, H. Jin, M. B. Sullivan and P. Wu, *Appl. Catal., A*, 2013, **451**, 79–85.
15 H. Öström, H. Öberg, H. Xin, J. LaRue, M. Beye, M. Dell'Angela, J. Gladh, M. L. Ng, J. A. Sellberg, S. Kaya, G. Mercurio, D. Nordlund, M. Hantschmann, F. Hieke, D. Kühn, W. F. Schlotter, G. L. Dakovski, J. J. Turner, M. P. Minitti, A. Mitra, S. P. Moeller, A. Föhlisch, M. Wolf, W. Wurth, M. Persson, J. K. Nørskov, F. Abild-Pedersen, H. Ogasawara, L. G. M. Pettersson and A. Nilsson, *Science*, 2015, **347**, 978–982.
16 O. Khalid, T. Weber, G. Drazic, I. Djerdj and H. Over, *J. Phys. Chem. C*, 2020, **124**, 18670–18683.
17 B. Qiao, A. Wang, X. Yang, L. F. Allard, Z. Jiang, Y. Cui, J. Liu, J. Li and T. Zhang, *Nat. Chem.*, 2011, **3**, 634–641.
18 L. Nie, D. Mei, H. Xiong, B. Peng, Z. Ren, X. I. P. Hernandez, A. DeLaRiva, M. Wang, M. H. Engelhard, L. Kovarik, A. K. Datye and Y. Wang, *Science*, 2017, **358**, 1419–1423.
19 T. Kropp and M. Mavrikakis, *ACS Catal.*, 2019, **9**, 6864–6868.
20 J. Hu, W. Liu, C. Xin, J. Guo, X. Cheng, J. Wei, C. Hao, G. Zhang and Y. Shi, *J. Mater. Chem. A*, 2021, **9**, 24803–24829.
21 Z. Zhu, H. Yin, Y. Wang, C.-H. Chuang, L. Xing, M. Dong, Y.-R. Lu, G. Casillas-Garcia, Y. Zheng, S. Chen, Y. Dou, P. Liu, Q. Cheng and H. Zhao, *Adv. Mater.*, 2020, **32**, 2004670.
22 X. Li, P. Cui, W. Zhong, J. Li, X. Wang, Z. Wang and J. Jiang, *ChemComm*, 2016, **52**, 13233–13236.
23 S. Dou, C.-L. Dong, Z. Hu, Y.-C. Huang, J.-l. Chen, L. Tao, D. Yan, D. Chen, S. Shen, S. Chou and S. Wang, *Adv. Funct. Mater.*, 2017, **27**, 1702546.
24 Y. Xue, B. Huang, Y. Yi, Y. Guo, Z. Zuo, Y. Li, Z. Jia, H. Liu and Y. Li, *Nat. Commun.*, 2018, **9**, 1460.
25 X.-P. Yin, H.-J. Wang, S.-F. Tang, X.-L. Lu, M. Shu, R. Si and T.-B. Lu, *Angew. Chem., Int. Ed.*, 2018, **57**, 9382–9386.
26 X.-F. Yang, A. Wang, B. Qiao, J. Li, J. Liu and T. Zhang, *Acc. Chem. Res.*, 2013, **46**, 1740–1748.
27 S. Lin, X. Ye, R. S. Johnson and H. Guo, *J. Phys. Chem. C*, 2013, **117**, 17319–17326.
28 S. Wang, J. Li, Q. Li, X. Bai and J. Wang, *Nanoscale*, 2020, **12**, 364–371.
29 E. W. McFarland and H. Metiu, *Chem. Rev.*, 2013, **113**, 4391–4427.
30 J. Liu, *ACS Catal.*, 2017, **7**, 34–59.
31 Y.-H. Lu, M. Zhou, C. Zhang and Y. P. Feng, *J. Phys. Chem. C*, 2009, **113**, 20156–20160.
32 E. H. Song, Z. Wen and Q. Jiang, *J. Phys. Chem. C*, 2011, **115**, 3678–3683.
33 Y. Tang, W. Chen, H. Chai, G. Zhao, Y. Li, D. Ma and X. Dai, *J. Phys. Chem. C*, 2019, **123**, 10926–10939.
34 K. Mao, L. Li, W. Zhang, Y. Pei, X. C. Zeng, X. Wu and J. Yang, *Sci. Rep.*, 2014, **4**, 5441.
35 S. Manzeli, D. Ovchinnikov, D. Pasquier, O. V. Yazyev and A. Kis, *Nat. Rev. Mater.*, 2017, **2**, 17033.
36 K. F. Mak, C. Lee, J. Hone, J. Shan and T. F. Heinz, *Phys. Rev. Lett.*, 2010, **105**, 136805.
37 J. Mao, Y. Wang, Z. Zheng and D. Deng, *Front. Phys.*, 2018, **13**, 138118.
38 Q. H. Wang, K. Kalantar-Zadeh, A. Kis, J. N. Coleman and M. S. Strano, *Nat. Nanotechnol.*, 2012, **7**, 699–712.
39 Y. Fan, J. Zhang, Y. Qiu, J. Zhu, Y. Zhang and G. Hu, *Comput. Mater. Sci.*, 2017, **138**, 255–266.
40 D. Ma, W. Ju, T. Li, X. Zhang, C. He, B. Ma, Z. Lu and Z. Yang, *Appl. Surf. Sci.*, 2016, **383**, 98–105.
41 D. Ma, W. Ju, T. Li, G. Yang, C. He, B. Ma, Y. Tang, Z. Lu and Z. Yang, *Appl. Surf. Sci.*, 2016, **371**, 180–188.
42 Y.-Y. Chen, M. Dong, J. Wang and H. Jiao, *J. Phys. Chem. C*, 2010, **114**, 16669–16676.
43 S. Liu and S. Huang, *Appl. Surf. Sci.*, 2017, **425**, 478–483.
44 D. Ma, Y. Tang, G. Yang, J. Zeng, C. He and Z. Lu, *Appl. Surf. Sci.*, 2015, **328**, 71–77.
45 A. Sharma, A. Srivastava, M. Husain and M. S. Khan, *J. Mater. Sci.*, 2018, **53**, 9578–9588.
46 Q. Ma, P. M. Odenthal, J. Mann, D. Le, C. S. Wang, Y. Zhu, T. Chen, D. Sun, K. Yamaguchi, T. Tran, M. Wurch, J. L. McKinley, J. Wyrick, K. Magnone, T. F. Heinz, T. S. Rahman, R. Kawakami and L. Bartels, *J. Phys.: Condens. Matter*, 2013, **25**, 252201.
47 H.-P. Komsa, J. Kotakoski, S. Kurasch, O. Lehtinen, U. Kaiser and A. V. Krasheninnikov, *Phys. Rev. Lett.*, 2012, **109**, 035503.
48 H.-P. Komsa, S. Kurasch, O. Lehtinen, U. Kaiser and A. V. Krasheninnikov, *Phys. Rev. B: Condens. Matter Mater. Phys.*, 2013, **88**, 035301.
49 G. Liu, A. W. Robertson, M. M.-J. Li, W. C. H. Kuo, M. T. Darby, M. H. Muhieddine, Y.-C. Lin, K. Suenaga, M. Stamatakis, J. H. Warner and S. C. E. Tsang, *Nat. Chem.*, 2017, **9**, 810–816.

50 T. Jitwatanasirikul, T. Roongcharoen, C. Chitpakdee, S. Jungsuttiwong, P. Poldorn, K. Takahashi and S. Namuangruk, *New J. Chem.*, 2021, **45**, 17407–17417.

51 P. E. Blöchl, *Phys. Rev. B: Condens. Matter Mater. Phys.*, 1994, **50**, 17953–17979.

52 G. Kresse and D. Joubert, *Phys. Rev. B: Condens. Matter Mater. Phys.*, 1999, **59**, 1758–1775.

53 G. Kresse and J. Furthmüller, *Comput. Mater. Sci.*, 1996, **6**, 15–50.

54 J. P. Perdew, K. Burke and M. Ernzerhof, *Phys. Rev. Lett.*, 1996, **77**, 3865–3868.

55 S. Grimme, S. Ehrlich and L. Goerigk, *J. Comput. Chem.*, 2011, **32**, 1456–1465.

56 B. Uberuaga and H. Jonsson, *J. Chem. Phys.*, 2000, **113**, 9901–9904.

57 G. Henkelman and H. Jónsson, *J. Chem. Phys.*, 1999, **111**, 7010–7022.

58 J. Kästner and P. Sherwood, *J. Chem. Phys.*, 2008, **128**, 014106.

59 D. Yang, S. J. Sandoval, W. M. R. Divigalpitiya, J. C. Irwin and R. F. Frindt, *Phys. Rev. B: Condens. Matter Mater. Phys.*, 1991, **43**, 12053–12056.

60 M. Chen, X.-B. Yang, J. Cui, J.-J. Tang, L.-Y. Gan, M. Zhu and Y.-J. Zhao, *Int. J. Hydrogen Energy*, 2012, **37**, 309–317.

61 G. Henkelman, A. Arnaldsson and H. Jónsson, *Comput. Mater. Sci.*, 2006, **36**, 354–360.

62 G. Xu, R. Wang, Z. Lu, D. Ma and Z. Yang, *J. Phys. Chem. C*, 2018, **122**, 23481–23492.

63 F. Li and Z. Chen, *Nanoscale*, 2018, **10**, 15696–15705.

64 Y. Tang, Z. Yang and X. Dai, *Phys. Chem. Chem. Phys.*, 2012, **14**, 16566–16572.

65 M. D. Esrafili, P. Nematollahi and R. Nurazar, *Superlattices Microstruct.*, 2016, **92**, 60–67.

66 Y.-H. Lu, M. Zhou, C. Zhang and Y. P. Feng, *J. Phys. Chem. C*, 2009, **113**, 20156–20160.

67 M. D. Esrafili and S. Asadollahi, *ChemistrySelect*, 2018, **3**, 9181–9188.

68 Z. Lu, P. Lv, J. Xue, H. Wang, Y. Wang, Y. Huang, C. He, D. Ma and Z. Yang, *RSC Adv.*, 2015, **5**, 84381–84388.

69 Y. Tang, X. Dai, Z. Yang, L. Pan, W. Chen, D. Ma and Z. Lu, *Phys. Chem. Chem. Phys.*, 2014, **16**, 7887–7895.

70 G. Xu, R. Wang, Y. Ding, Z. Lu, D. Ma and Z. Yang, *J. Phys. Chem. C*, 2018, **122**, 23481–23492.